PNAS RESEARCH ARTICLE | CELL BIOLOGY
BIOPHYSICS AND COMPUTATIONAL BIOLOGY

Endosomal membrane budding patterns in plants

Ethan Weiner[a,1], Elizabeth Berryman[a,1], Felix Frey[b,1], Ariadna González Solís[a,1], André Leier[c], Tatiana Marquez Lago[c], Anđela Šarić[b], and Marisa S. Otegui[a,2]

Affiliations are included on p. 11.

Edited by Eugenia (Jenny) Russinova, Universiteit Gent, Ghent, Belgium; received May 13, 2024; accepted September 7, 2024

Multivesicular endosomes (MVEs) sequester membrane proteins destined for degradation within intralumenal vesicles (ILVs), a process mediated by the membrane-remodeling action of Endosomal Sorting Complex Required for Transport (ESCRT) proteins. In *Arabidopsis*, endosomal membrane constriction and scission are uncoupled, resulting in the formation of extensive concatenated ILV networks and enhancing cargo sequestration efficiency. Here, we used a combination of electron tomography, computer simulations, and mathematical modeling to address the questions of when concatenated ILV networks evolved in plants and what drives their formation. Through morphometric analyses of tomographic reconstructions of endosomes across yeast, algae, and various land plants, we have found that ILV concatenation is widespread within plant species, but only prevalent in seed plants, especially in flowering plants. Multiple budding sites that require the formation of pores in the limiting membrane were only identified in hornworts and seed plants, suggesting that this mechanism has evolved independently in both plant lineages. To identify the conditions under which these multiple budding sites can arise, we used particle-based molecular dynamics simulations and found that changes in ESCRT filament properties, such as filament curvature and membrane binding energy, can generate the membrane shapes observed in multiple budding sites. To understand the relationship between membrane budding activity and ILV network topology, we performed computational simulations and identified a set of membrane remodeling parameters that can recapitulate our tomographic datasets.

ESCRT | multivesicular endosomes | vesiculation

Significance

Plant endosomes show unique membrane vesiculation patterns among eukaryotes, forming complex arrays of interconnected vesicles containing plasma membrane proteins targeted for degradation. Endosomal Sorting Complex Required for Transport (ESCRT) proteins mediate endosomal vesicle formation, yet the evolutionary origins of these unique mechanisms in plants remain unclear. Our cross-species structural analyses revealed widespread endosomal vesicle concatenation in land plants, particularly prevalent in seed plants. We identified multiple endosomal budding domains with several interlinked vesicles forming simultaneously, only in hornworts and seed plants, suggesting an independent evolutionary origin of this mechanism in these plant lineages. Computational simulations show that changes in ESCRT filament curvature and membrane binding energy can mediate the formation of concatenated vesicles and multiple budding sites.

Cells continually perceive external and internal stimuli through surface receptors, channels, and lipids in their plasma membrane. The ability to regulate the plasma membrane composition is crucial for cell survival and, in multicellular organisms, for proper development and physiological responses. The degradation of plasma membrane proteins occurs in lysosomes/vacuoles and is mediated by the endocytic/endosomal pathway. Plasma membrane proteins targeted for degradation by ubiquitination are sorted and internalized into endocytic vesicles, which are in turn delivered to early endosomes (1). Endocytosed, ubiquitinated proteins are retained in the endosomal system and as early endosomes mature into multivesicular endosomes (MVEs), ubiquitinated cargo proteins at the endosomal limiting membrane are sequestered within intralumenal vesicles (ILVs) that bud into the endosomal lumen. The fusion of MVEs with vacuoles results in the degradation of ILVs and their cargo proteins by hydrolytic enzymes.

During ILV formation, the endosomal membrane domain containing cargo proteins bends away from the cytosol, that is, in the opposite topology of other better-characterized vesiculation events, such as those producing secretory vesicles in the Golgi or endocytic vesicles at the plasma membrane. Consistently, ILVs are formed by a specialized group of proteins called Endosomal Sorting Complex Required for Transport (ESCRT), which orchestrate both the clustering of ubiquitinated cargo proteins and induce the deformation of the endosomal membrane away from the cytoplasm (negative membrane bending) and into the endosomal lumen (2–5).

ESCRT proteins are an ancient machinery present in all domains of life (6). Beyond their role in MVE sorting and vesiculation, their functions also include various membrane deformation events of similar negative topology (7). Disruption of core ESCRT function has lethal consequences in multicellular organisms (8–15). However, how exactly ESCRTs remodel membranes is not completely understood. Most eukaryotes have five multimeric ESCRT complexes (ESCRT-0 to III and SKD1/VPS4-LIP5), with early ESCRTs binding and recruiting ubiquitinated cargo and later ESCRTs mediating membrane deformation and ILV budding (2).

There are seven conserved ESCRT-III proteins known to act on endosomal budding: VPS20, SNF7, VPS24, VPS2, CHMP1, VPS60, and IST1 (4, 16–18). ESCRT-III

Author contributions: E.W., E.B., F.F., A.G.S., A.L., T.M.L., A.Š., and M.S.O. designed research; E.W., E.B., F.F., A.G.S., A.L., T.M.L., A.Š., and M.S.O. performed research; E.W., E.B., F.F., A.G.S., A.L., T.M.L., A.Š., and M.S.O. analyzed data; and E.W., E.B., F.F., A.G.S., A.L., T.M.L., A.Š., and M.S.O. wrote the paper.

The authors declare no competing interest.

This article is a PNAS Direct Submission.

[1]E.W., E.B., F.F., and A.G.S. contributed equally to this work.

[2]To whom correspondence may be addressed. Email: otegui@wisc.edu.

This article contains supporting information online at https://www.pnas.org/lookup/suppl/doi:10.1073/pnas.2409407121/-/DCSupplemental.

Published October 23, 2024.

proteins polymerize in filaments on the surface of the endosomal membrane. Based on structural and biophysical models, ESCRT-III proteins have been postulated to first assemble in flat filamentous spirals enriched in SNF7 (19, 20) and transition into three-dimensional arrays that lead to membrane buckling and the constriction of the ILV bud neck (21–23). Although all eukaryotic organisms contain ESCRT proteins, plant ESCRTs have specific features, including the occurrence of plant-specific ESCRT subunits and a large diversification of ESCRT-III components (24), raising the possibility that the ESCRT polymer transitions that mediate endosomal membrane deformation could differ between plants and other organisms.

While it is widely accepted that ESCRT-III plays a pivotal role in membrane deformation during ILV bud formation, the mechanism of membrane fission remains more controversial. Membrane-remodeling mechanisms by ESCRT proteins are traditionally studied under the assumption that ILVs are released individually and that ESCRT proteins are recycled by the AAA ATPase VPS4 (known as SKD1 in plants) back to the cytoplasm (25), direct documentation of individual ILV release from endosomal membranes has remained elusive. This challenge stems from the small size of ILVs (35 to 50 nm) forming in highly mobile endosomes, which drastically limits the opportunities for direct visualization. Based on an electron tomography analysis, we have previously shown that in *Arabidopsis thaliana* root cells, ILVs form as interconnected networks that largely do not undergo scission (26). The presence of the ESCRT-III subunit SNF7 in intervesicular membranous bridges suggests that constricted ESCRT-III filaments are not recycled from the endosomal membrane during the formation of plant ILVs and are instead delivered to vacuoles together with the ILVs (26). Concatenated ILVs can form from single or multiple budding sites characterized by ILV buds interconnected by lateral membrane bridges. The presence of ESCRTs at intervesicular bridges and ILV bud necks could serve as diffusion barriers, facilitating cargo sequestration within endosome lumenal membranes (26).

Whether ILV concatenation is restricted exclusively to plants and how and when it evolved within the plant lineage is unknown. Here, we conducted electron tomographic analyses of MVEs and their ILVs in multiple plant lineages, yeast, and algae to determine the occurrence of ILV concatenation and multiple budding and therefore, to better understand the function of ESCRT proteins across species. We developed computer simulations to understand the biophysical properties of ESCRT proteins able to mediate ILV concatenation and multiple budding in plant MVEs as well as to predict the parameters that underlie the different topologies of ILV networks. Our results support the notion that changes in the properties of ESCRT-III filaments could have drastically changed endosomal vesiculation patterns in plants.

Results

Morphometric Analysis and ILV Concatenation Patterns of Plant MVEs. To analyze the degree of vesicle concatenation and the general structural features of MVEs across plant lineages, we collected vegetative tissues from representative species of the major clades of land plants as well as *Chara braunii* as a representative of Charophyte algae (one of the closest algal relative to land plants) (27), and *Saccharomyces cerevisiae* (budding yeast) as a nonphotosynthetic organism. Samples included haploid thalli of *Ch. braunii*, *Marchantia polymorpha (*liverwort), and *Anthoceros sp.* (hornwort) as well as diploid root cortical cells of *Selaginella kraussiana (*lycophyte), *Pteris cretica* (Cretan brake fern), *Pinus resinosa* (red pine), *Amborella trichocarpa*, *Nymphaea odorata* (water lily), *Zea mays* (maize), and *A. thaliana*. Tissues were high-pressure frozen, freeze substituted, resin-embedded, and imaged by dual-axis electron tomography. We reconstructed and segmented between 3 and 10 MVEs for each species (Fig. 1*A*).

We first determined the average sizes of MVEs and their ILVs for each species. The smallest MVEs were found in *Saccharomyces* (av. diam. 251 nm) and the largest, in *Pinus* cells (av. diam. 484 nm; Fig. 1*B*). ILVs in *Chara* and all plants were larger than yeast ILVs (av. diam. 32 nm) and ranged from 35 nm in *Arabidopsis* to 46 nm in *Pinus* (Fig. 1*C*). *Zea* and *Arabidopsis* MVEs contain ILVs fairly uniform in size; however, just like reported for mammalian cells (28), all other species contained two types of ILVs based on appearance and size: a population of large ILVs with translucent contents (4.5% of *Saccharomyces* ILVs to 21% in *Selaginella* ILVs; av. diam. between 44 nm in *Saccharomyces* to 60 nm in *Chara* and *Selaginella*) and a more abundant population of smaller ILVs with electron-dense contents (av. diam. ranging from 31 nm in *Saccharomyces* to 43 nm in *Pinus*) (Fig. 1 *C* and *D*).

We next analyzed whether ILVs in different plant lineages are concatenated as previously reported in *Arabidopsis* cells (29, 30). To compare among species, we classified each ILV contained in our MVE tomographic reconstructions in one of three categories: ILVs physically connected to others through membrane bridges ("concatenated ILVs"), free ILVs in the MVE lumen ("free ILVs"), or single budding ILVs still connected to the MVE limiting membrane ("single bud") (Fig. 1*E*). Between 16% and 13% of the ILVs were concatenated in *Saccharomyces* and *Chara,* respectively. However, within land plants the occurrence of ILV concatenation was higher, ranging from 36 to 37% in early divergent land plants such as *Marchantia*, *Selaginella*, and *Pteris*, to 83% and 91% in MVEs of *Arabidopsis* and *Nymphaea*, respectively. Interestingly, *Anthoceros* MVEs showed 87% ILV concatenation, a pattern more commonly found within flowering plants than in the early divergent clades (Fig. 1*E*). Both small and large ILVs were found in concatenated networks in plants, so we consider them together in all our subsequent analyses.

Although all analyzed plant species showed concatenated ILVs, their ILV networks differ in topology and complexity, based on the number of membranous bridges interconnecting ILVs, the number of ILVs still connected to the limiting membrane (active budding sites), and the total number of ILVs contained in a network. This suggests that the mechanisms of ILV formation may differ across plant species. To better understand variations in topology of the ILV networks, we depicted them in two dimensions for analysis (Fig. 2 *A*–*C* and *SI Appendix*, Fig. S1).

There was a clear predominance of linear ILV chains in early divergent plant groups, progressively transitioning into more complex networks in seed plants (*Pinus* and flowering plants) (*SI Appendix*, Fig. S1). As a proxy of ILV network complexity, we quantified the number of membranous bridges connected to each ILV. Thus, a value of 0 corresponded to a free vesicle with no membranous bridges, 1 to a terminal ILV or a single bud, 2 to an ILV with two membranous bridges, and so on, with the highest value of 6 detected in *Nymphaea* ILVs (*SI Appendix*, Fig. S2*A*). We then calculated the average number of membranous bridges per ILV for each of the 11 species under analysis (Fig. 2*D*). While *Chara* and *Saccharomyces* had an average of 0.15 and 0.25 bridges per ILV, respectively, consistent with over 75% of their ILVs being free, there was a progressive increase in this parameter across the phylogenetic tree of plants, with 0.54 and 0.6 bridges per ILV in *Marchantia* and *Selaginella*, respectively, 0.91 in *Pinus*, and 1.8 and 2.3 in *Arabidopsis* and *Nymphaea*, respectively. Once again, *Anthoceros* MVEs were outliers showing 1.5 bridges per ILV, a

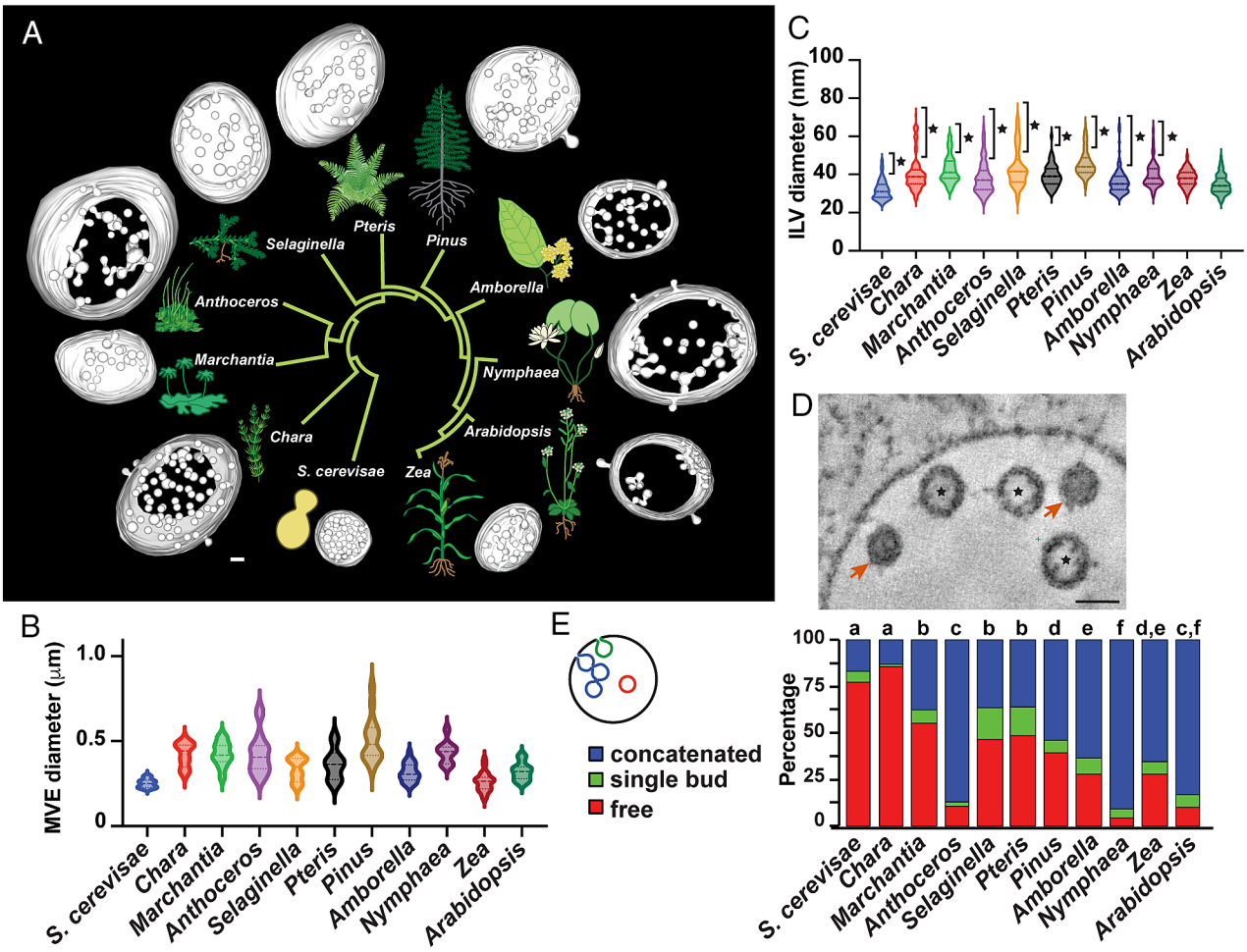

Fig. 1. MVEs in land plants. (*A*) Tomographic reconstructions from representatives of the major clades of land plants as well as budding yeast and *Chara*. (*B*) Quantitative analysis of MVE diameter across species. (*C*) Quantitative analysis of ILV diameter. Most species show ILVs that fall into two types based on their sizes and content electron-density. Asterisks indicate the population of ILVs of larger size and translucent lumen. (*D*) Example of two types of ILVs in *M. polymorpha*; asterisks indicate large, electron-translucent ILVs whereas red arrows point at smaller, electron-dense ILVs. (*E*) Percentage of concatenated, free, and single ILV buds across species. Different letters on graphs indicate significant difference ($P < 0.05$) calculated by a chi-squared test. (Scale bars, 50 mm).

value more commonly found among flowering plants than in early divergent plant groups (Fig. 2*E* and *SI Appendix*, Fig. S2*A*).

Based on the analysis of *Arabidopsis* MVEs, membranous bridges connecting ILVs are likely established as ESCRT proteins deform the MVE limiting membrane during the formation of ILVs (29). These ILVs can form from single budding sites that give rise to linear ILV chains or from multiple budding sites in which ILV buds share lateral membranous bridges and give rise to complex networks of concatenated ILVs (29) (*SI Appendix*, Fig. S2*B*). We quantified in our tomograms the number of interconnected ILVs in budding sites as a parameter we called "multiplicity." The majority of budding sites across all species had a multiplicity of 1 (single budding sites; *SI Appendix*, Fig. S2*C*). Surprisingly, budding sites with a multiplicity of 2 or greater ("multiple budding sites") were only found in the seed-bearing species (*Pinus*, *Amborella*, *Nymphaea, Zea,* and *Arabidopsis)*, with the notable exception of *Anthoceros*.

Assuming that the membranous bridges are fairly stable and persist after the formation of the ILVs, the topology of the ILV networks should recapitulate the processive budding activity at the MVE limiting membrane. In this case, one would expect that the number of bridges per ILV correlates with the number of interconnected ILVs in the budding sites from where they have originated. For example, a single budding site can only generate a linear chain of ILVs, with up to two membranous bridges per ILV, whereas a double budding site can generate ILVs with up to three bridges (*SI Appendix*, Fig. S2*B*). Thus, the highest possible number of membranous bridges per ILV corresponds to the number of ILVs engaged in that particular budding event plus 1.

To test whether indeed the multiplicity of budding sites predicts the number of bridges per ILV, we plotted the average values of both parameters (Fig. 2*E*). Because it is impossible for budding sites to have a multiplicity of less than one, this value served as a baseline. We found a strong positive correlation between the two variables for plant MVEs. A linear regression analysis of multiplicity (x) and average number of bridges per ILV (y) shows a relationship of $y = 1.33\,x - 0.65$ with an R^2 value of 0.94, assuming $x \geq 1$. However, the average numbers of bridges per ILV were always far beneath the expected higher limit (multiplicity +1), suggesting that, although both parameters are correlated, losses of bridges or other dynamic changes occur during the formation of ILV networks.

To test whether the structural features observed in plant MVEs are characteristic of specific taxa or instead, vary widely according to cell types and cellular functions, we also analyzed MVEs from a functionally different cell type, *Arabidopsis* tapetal cells, which become multinucleate and are specialized in secretion (31). In terms of multiplicity and number of bridges per ILV, the MVEs in both *Arabidopsis* root cortical cells and tapetum were very similar (*SI Appendix*, Figs. S1 and S2 *A* and *C*), supporting the notion

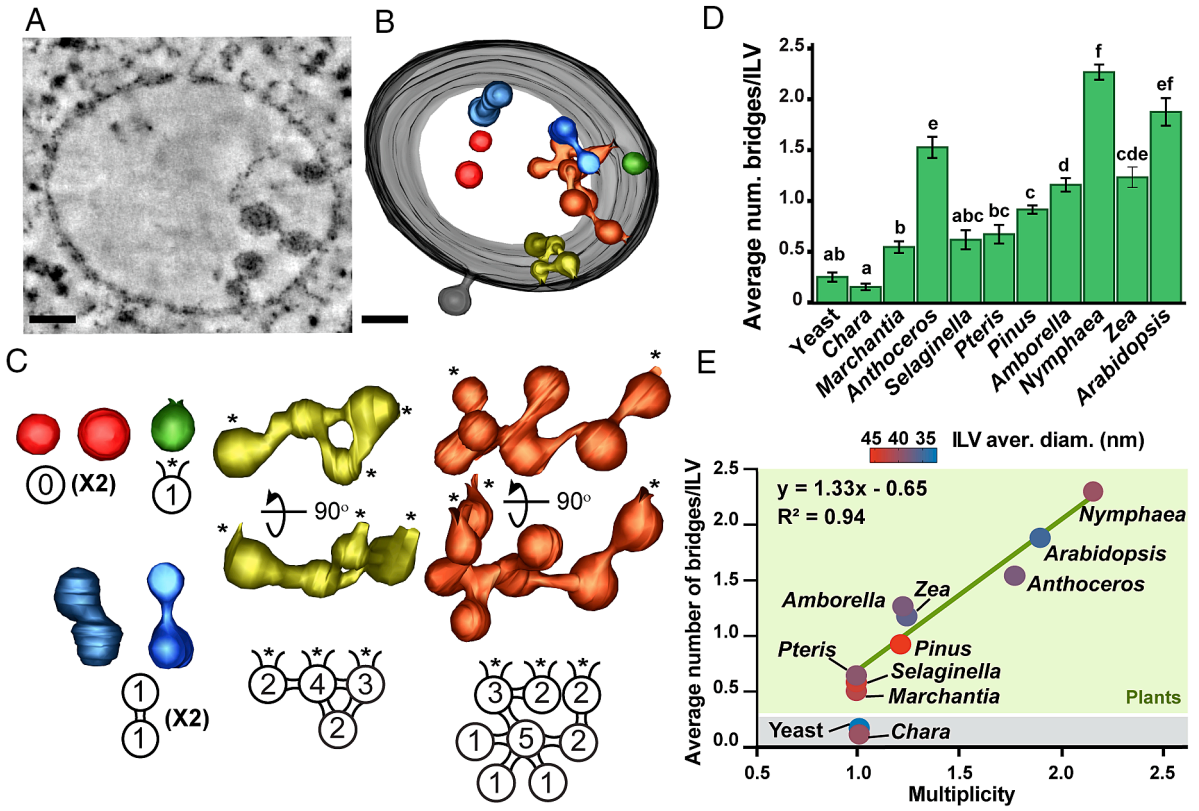

Fig. 2. Representative examples of ILV analysis in MVEs of *Arabidopsis* root cells. (*A*) Tomographic slice and (*B*) tomographic reconstruction of an MVE with discrete ILV networks and free ILVs depicted in different colors. (*C*) Free ILVs, single buds, and concatenated ILV networks from MVE shown in (*A*) and (*B*), were analyzed separately and depicted as 2D simplified topologies, with ILVs represented by circles and membranous bridges, by lines between ILVs. Asterisks indicate bridges still connected to the limiting membrane (budding site) and the number inside each ILV reflects the number of membranous bridges connected to it. Parentheticals indicate the number of times a given topology was found in the reconstructed MVE. (*D*) Graph of average number of membranous bridges per ILV in the species under study. Different letters on graphs indicate significant difference ($P < 0.05$) calculated by one-way ANOVA followed by Tukey's test. (*E*) Graph depicting the average number of bridges per ILV against the average number of ILVs in budding sites (multiplicity). Regression analysis between the two variables retrieved an R^2 value of 0.94. The color of each circle represents the average ILV diameter for that species.

that the structural complexity of plant MVEs are characteristic of taxa rather than their specific functions or cell type. We also considered whether the number of membranous bridges was correlated to the average diameter of ILVs, based on the idea that large ILVs could bear more bridges. However, that did not seem to be the case, as the ILVs with the higher number of bridges, such as those from *Nymphaea* and *Arabidopsis,* show intermediate or small diameters in comparison to ILVs from all the species under analysis (Fig. 2*E*). These results suggest that ILV network topology within MVEs varies widely across taxa and not among cell types or MVEs with different ILV sizes.

Molecular Dynamics Simulations of ILV Budding in Plants. To investigate the putative biophysical determinants that could explain the peculiar mechanisms of ILV formation in plant MVEs, we performed particle-based coarse-grained molecular dynamics simulations. In the simulations, we modeled the endosomal membrane, ESCRT filaments, and ILV cargo. To simulate the endosomal bilayer membrane we made use of a previously developed computational model (32), in which a membrane patch of ~10 nm^2 was represented by a membrane bead. The interaction between membrane beads was mediated by an anisotropic pair potential whose strength depended on both the distance between membrane beads and the bead orientation, giving rise to a fluid lipid membrane with a bending rigidity $\kappa \sim 20\ k_BT$ (32). To model membrane remodeling by ESCRT filaments, we used our previously developed computational model for ESCRT filaments (33). In the model, an ESCRT filament consisted of connected subunits (monomers) which are formed of three beads, distributed along the corners of an equilateral triangle (Fig. 3*A*). The beads of the neighboring subunits interact with each other through bonds, mediated through distance-dependent harmonic potentials. In general, the geometry of the ESCRT filament was a ring, spiral, or helix described by the angle α between subunits or the radius R, and the tilt angle τ between the ESCRT filament and the membrane (Fig. 3*A*); $\tau = 0°$ corresponds to a flat filament, $0° < \tau < 90°$ corresponds to a conical filament, and $\tau = 90°$ corresponds to a cylindrical filament configuration. ESCRT filaments adhered along the two beads at the base of the filament to membrane beads (blue beads in Fig. 3*A*), controlled through the adhesion strength $\epsilon_{ema.}$ The ILV cargo (e.g., integral membrane proteins) was simulated as spheres that adhered to membrane beads but did not undergo full passive wrapping. The model parameters are summarized in *SI Appendix*, Table S1. Further details on the computational model can be found in the *Methods* section and in *SI Appendix*, *Supplemental Methods*.

We effectively integrated the equations of motion in the *NpT (constant-particle number*, constant-temperature, constant-pressure) ensemble coupled to a Langevin thermostat. We controlled $p = 0$, mimicking vanishing membrane tension. In the simulation, the parameters for membrane and cargo properties were held constant; however, we allowed the ESCRT filament properties to change during the runtime of the simulation, as we assumed ESCRT-III subunit turnover/exchange to occur during ILV formation (23). Thus, we introduced changes in the adhesion energy ϵ_{ema}, the angle α between subunits or radius R and the tilt angle τ. To allow for

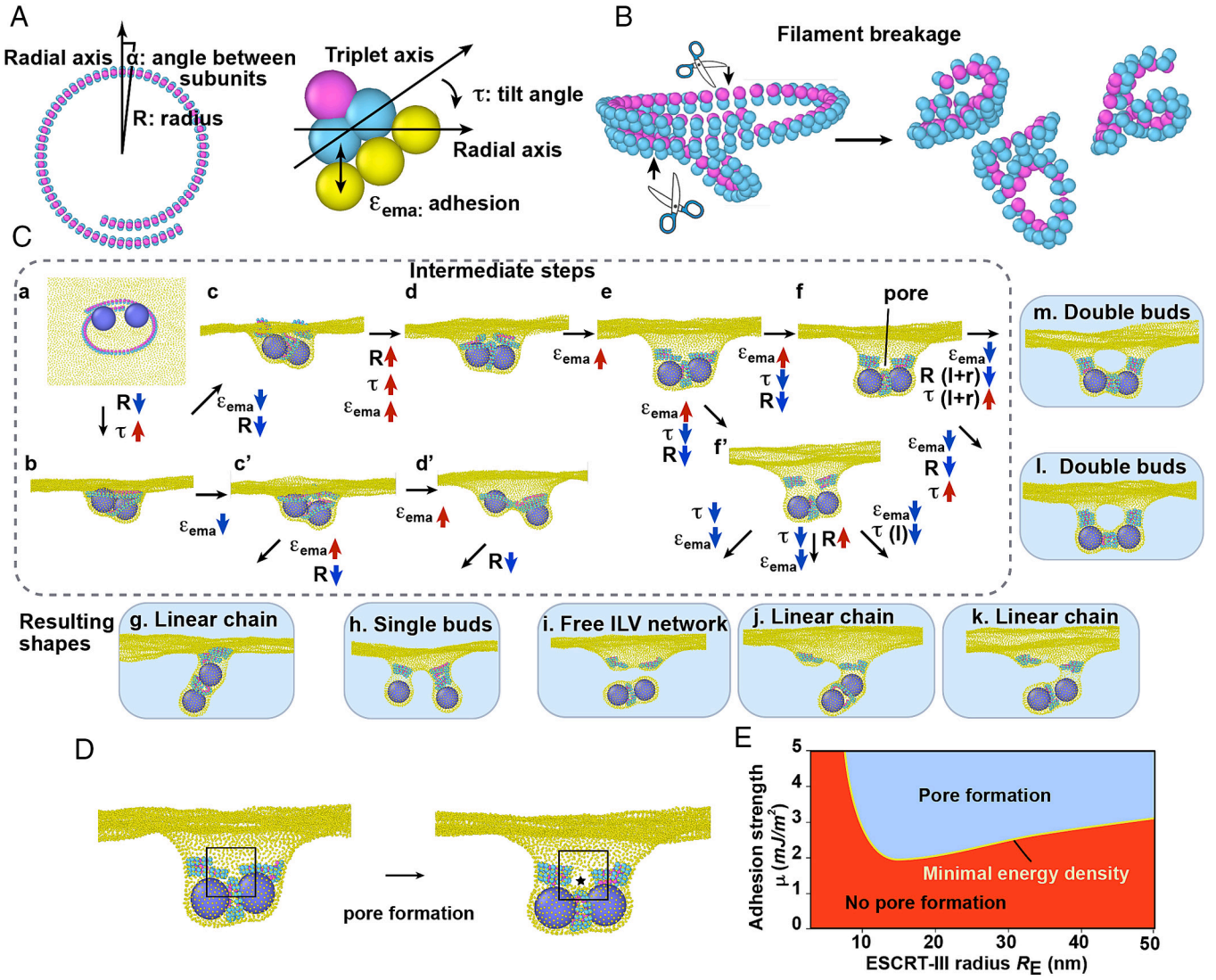

Fig. 3. Simulation of changes in ESCRT filament geometries and associated membrane deformation during formation of concatenated ILV networks. (*A*) ESCRT-III filaments of radius *R* consist of interconnected three-beaded subunits with the angle α between subunits (*Left*). The membrane-binding faces are depicted in blue and the strength of the adhesion is controlled by ϵ_{ema} (*Right*). The angle τ is the angle established between the radial axis and the triplet subunit axis. A τ value larger than 0° defines the tilted state of the filament. (*B*) During the simulation, the filament was allowed to break into 2 or more independent filaments. (*C*) Snapshots of the membrane and ESCRT-III filament intermediates during the formation of concatenated ILVs following different possible pathways. The changes of the filament properties (adhesion energy ϵ_{ema}, the α angle between subunits or the filament radius, and the tilt angle τ) during the simulation are indicated between intermediate simulation steps. In most cases, properties changed equally for all filaments. Only during the transition between the f and m states, the radius of the left and right filaments R(l + r) decreased and the tilt angle of the left and right filaments τ(l + r) increased, while the filament properties of the lower filament remained constant. Similarly, during the transition between the states f' and k, the tilt angle of the left filament τ(l) decreased, while the adhesion energy of all three filaments increased. The combination of parameter changes resulted in single buds (h), three types of linear ILV chains (g, j, k), free ILV networks (i), and two types of double budding sites (l and m). Also Movie S1. (*D*) Formation of a pore in a simulated double budding site. (*E*) Continuum model for pore formation in double budding sites. Condition for membrane pore formation due to ESCRT filament adhesion according to Eq. **1**. The solid yellow line marks the minimal adhesion energy density of ESCRT filaments μ as a function of the preferred ESCRT radius R_E so that membrane pore formation becomes energetically favorable. In the blue region, membrane pore formation is energetically favorable while in the red region membrane pore formation is energetically unfavorable.

multiple membranous bridges to form, we assumed that the ESCRT filament can fragment into shorter filaments during the simulation time. For simplicity, we assumed that the fragments have the same length (Fig. 3*B*).

We designed the simulation to test whether two ILVs forming in close proximity would generate concatenated patterns. For this, we initially placed two cargo spheres on the membrane and surrounded them by a single ESCRT filament (Fig. 3*C*, stage a). During the first simulation stage, the ESCRT filament radius decreased (mediated by an increasing value of α) and the tilt angle τ increased (Fig. 3*C*, stage b). We then introduced two cuts in the ESCRT filament; the three resulting filaments decreased their adhesion energy and opened two possible pathways depending on whether the filaments contracted further (Fig. 3*C*, stage c) or remained unchanged (Fig. 3*C*, stage c').

When the curvature of ESCRT filaments remained unchanged (Fig. 3*C*, stage c'), the simulation generated either a linear ILV chain (Fig. 3*C*, stage g) or two single buds (Fig. 3*C*, stage h; Movie S1), depending on the ESCRT filaments constricting earlier or later in the process, respectively. In both cases, only two ILV-associated membranous tubules formed, one with one and one with two ESCRT filaments.

Alternatively, when the ESCRT filaments contracted strongly (Fig. 3*C*, stage c) and both the tilt angle and membrane adhesion energy increased (Fig. 3*C*, stages d and e), two pathways were possible depending on the ESCRT filaments either adhering to

the membrane strongly (Fig. 3*C*, stage f) or less strongly (Fig. 3*C*, stage f'). If the adhesion to the membrane was strong and the filaments further constricted, a membrane pore opened, generating double budding sites of two kinds (Fig. 3*C*, stages l and m; Movie S1). One type of double budding site had three similar membranous bridges with all three ESCRT filaments constricted to the same size (Fig. 3*C*, stage l). The other kind of double budding site showed membranous bridges of different sizes with the two ESCRT filaments that connect the ILV to the membrane undergoing further constriction to a smaller radius compared to the third ESCRT filament between the ILVs (Fig. 3*C*, stage m). When the ESCRT filaments attached less strongly to the membrane, no membrane pore was formed (Fig. 3*C*, stage f'), and the simulation generated three different patterns, either two concatenated ILVs detached from the limiting membrane (free ILV network; Fig. 3*C*, stage i) if the filaments remained constricted, or two types of linear ILV chains (Fig. 3*C*, stages j and k). One type of linear ILV chain resulted from ESCRT filaments relaxing symmetrically whereas for the other linear ILV chain to form, the ESCRT filaments stayed constricted while the tilt angles decreased only for one of the two filaments associated with ILVs. All the parameter values required to generate the seven final configurations and their intermediates are included in *SI Appendix*, Table S2 and also shown in Movie S1.

Based on our tomographic data, the average length of the membranous bridges connecting ILVs between themselves and with the limiting membrane was 11 nm with a radius of 8 nm in *Arabidopsis* MVEs. The size of a bead in ESCRT filaments corresponded to 2.3 nm and set the length scale in our simulations (33). Then the thickness of the ESCRT filament was around 4.1 nm, the initial length was 159 nm and the resulting membranous bridges were approximately 14 nm in length with a radius of 9 nm. The typical vesicle diameter of an ILV bud in the simulation was approximately 23 nm (compared to the distribution of ILV diameters for *Arabidopsis* and other plant species in Fig. 1*C*). Thus, the dimensions of membranous bridges and ILV in our simulations were close to those found in plant MVEs. Moreover, the main energy barrier to the formation of these membrane shapes came from the membrane bending energy. In its analytical form, the bending energy depends on membrane shape but not necessarily on the size over which the curvature occurs. For example, the bending energy to wrap a sphere is $8\pi\kappa$ independent of sphere size (34). Hence, we do not expect to find major artifacts in the simulations because of dimensional mismatch.

Continuum Model of Pore Formation in Double Budding Sites. According to our simulations, a critical event in the formation of a double budding site and higher-order multiple budding sites as seen in flowering plants, is the breaking of the limiting membrane into a pore (Fig. 3*C*, stage f). To rationalize whether membrane pore formation driven by ESCRT-III filaments in ILV network formation is plausible, we studied a complementary continuum model. In the model, we analyzed the energy involved in generating such a pore by focusing on this specific membrane region, delineated by a box in Fig. 3*D*. In this region, having the shape of a membrane pit, there are two opposing membrane leaflets, one at the front and one at the back, and three ESCRT filaments. The model assumed that the central area of the membrane pit changed from a planar state to a pore state (Fig. 3*D*), driven by the adhesion of the three initially unbound ESCRT filaments to the membrane around the pore. In contrast, the shape of the membrane in the peripheral area was assumed to stay unchanged and was therefore not considered in this analysis. We compared the total energy of the initial state (1) with the total energy of the membrane in the state where a membrane pore has opened (2). In *SI Appendix*, the full analytical derivation is detailed.

Comparing the energy of the initial and final states (Fig. 3*D*) the pore state became energetically favorable if $E_1^{\text{total}} \geq E_2^{\text{total}}$. From the condition we obtained

$$\mu \geq \frac{2\pi(\pi-2)}{A}\kappa + \frac{2}{3R^2}\kappa + 2\kappa_E\left(\frac{1}{2R} - \frac{1}{R_E}\right)^2. \qquad [1]$$

In Eq. **1**, μ is the adhesion energy of the ESCRT filaments to the membrane, A is the surface area of the membranous bridge of cylindrical shape where an ESCRT filament is adsorbed onto the membrane, R is the radius of the cylindrical bridge, κ is the bending rigidity of the membrane, κ_E is the bending rigidity of the membrane to which ESCRT was adsorbed and RE is the preferred ESCRT filament radius.

The solid yellow line in Fig. 3*E* marks the minimal energy density needed for the formation of a pore, according to Eq. **1**, using typical parameter values for the length and radius of the membrane cylinders L = 11 nm and R = 8 nm, i.e., $A = 2\pi RL$ = 553 nm^2, a membrane rigidity of κ = 20 k_BT (35) and κ_E = 80 k_BT for the ESCRT filament rigidity, estimated from the filament rigidity of 260 nm k_BT of yeast ESCRT-III proteins (19). We found that pore formation was facilitated by increasing the membrane adhesion of ESCRT filaments for an intermediate ESCRT radius. By using Eq. **1** and the measured preferred radius of yeast ESCRT-III filaments (R_E = 25 nm; (19)) we estimated the adhesion strength of ESCRT filaments as μ = 2.25 mJ/m^2, necessary to break a membrane pore. The estimated value is similar to the adhesion energy density of single monomers of μ = 2.05 mJ/m^2, which we calculated from the binding energy per monomer (4 k_BT; (36)) divided by the monomer area a_0 = 8 nm^2, assuming a monomer length of 3.2 nm (19) and spherical shape. The observation suggests that ILV networks requiring membrane pores rely on ESCRT-III filaments that strongly adhere to the membrane. The estimated value is large compared to the previously reported value of μ = 0.31 mJ/m^2 for the polymerization energy density of Snf7 by Chiaruttini et al. (19). However, the parameter values assumed in our estimate may also vary. To show the effect, we used parameter values of L = 17 nm and R = 12 nm and κ = 8 k_BT, for which we obtained μ = 0.34 mJ/m^2, which is more consistent with the previously reported results.

Model of ILV Network Formation. Our analysis indicates that the budding activity at the MVE limiting membrane controls the topology of the ILV networks. Continuous budding from stable and unchanged budding sites would generate highly regular ILV networks where all ILVs would have predictable number of bridges (see for example the hypothetical ILV network generated by a double budding site in *SI Appendix*, Fig S2*B*). However, the ILV networks contained in our tomographic reconstruction are not regular (*SI Appendix*, Fig. S1) and their average number of bridges per ILV does not reach the values expected for permanent, unchangeable budding sites (Fig. 2*E*). We reasoned that, by recapitulating the stepwise formation of these ILV networks, we could uncover the associated dynamic changes in budding patterns at the limiting membrane. To this end, we generated a computational simulation to recapitulate ILV networks in the pine dataset, which contained 10 MVEs, 63 ILV networks with active budding sites (connected to the limiting membrane) and 154 ILVs (*SI Appendix*, Fig. S3). We found up to four bridges per

ILV and up to three interconnected ILV buds in budding sites (that is, multiplicity = 1, 2, and 3; *SI Appendix*, Fig. S3) in pine MVEs. The average number of ILVs per network in these 63 pine networks was 2.4 (±2.3 s.d.) whereas the average multiplicity of budding sites per network was 1.1 (±0.34 s.d.). We also measured the frequency of different types of budding sites in the 10 pine MVE tomograms: 0.921 for single (s1), 0.063 for double (s2), 0.016 for triple (s3) budding sites.

We then defined the possible events involved in ILV network formation. As membranous bridges contain ESCRT proteins (29), we assumed that they are formed at the limiting membrane during budding and not as part of membrane fusion intermediates between already formed ILVs. Thus, we considered that at the limiting membrane, an ILV budding site can either a) bud, pushing the old ILV bud into the lumen of the MVE and forming a new one connected to the limiting membrane (in the case of multiple budding sites, all ILV buds or only some of them can perform this action; Fig. 4*A*); b) bud with increasing multiplicity (for example, budding while going for a double into a triple budding site, Fig. 4*A*); or c) decrease in multiplicity by removing bridges with the limiting membrane (for example, going from a double budding site into a single budding site, Fig. 4*A*). We then estimated a probability for each of the three possible actions: budding (p1), budding plus increasing multiplicity (p2), and decreasing multiplicity (p3) (Fig. 4*A*), based on the budding site frequencies (s1 to s3) measured in our tomograms.

Computational simulations stopped when the network reached 14 ILVs (the largest network size that we observed in our tomographic data; *SI Appendix*, Fig. S3), or until a network disconnected from the limiting membrane. All intermediate and final networks were stored, and one was randomly chosen to represent the developing ILV network, similar to the snapshots that the EM data provided. We reasoned that the probabilities for the three parameters (p1 to p3) that resulted in ILV networks similar to the ones contained in our MVE tomographic reconstructions could reflect the budding patterns and activity of a pine MVE limiting membrane.

We conducted a parameter sweep for p1 to p3, with increments of 0.05. When comparing to the 63 pine ILV networks in terms of mean ILV number and mean budding site number, we found several parameter sets for which a Hotelling T^2 statistical test did not reject the null hypothesis that the mean statistics of simulated and tomography-reconstructed ILV networks are alike. In other words, the statistical test suggested that for such parameter sets the ILV networks obtained from our computational simulation were statistically indistinguishable from the pine EM data with respect to those two network characteristics. The parameter set with the highest *p*-value and lowest T^2 value were p1 = 0.55, p2 = 0.1, and p3 = 0.35 (Dataset S1), for budding, budding with increasing multiplicity, and decreasing multiplicity, respectively ($P = 0.994$; $T^2 = 0.013$).

Next, we chose p1 = 0.55, p2 = 0.1, p3 = 0.35 as our parameter set and ran 1,000 sets of 63 simulations each to be compared to the 63 tomography-reconstructed ILV networks (Dataset S2). We plotted the 1,000 simulation sets as histograms based on average number and SD of both number of ILVs/networks and multiplicity of budding sites/networks and determined where our tomography-reconstructed networks fit into this distribution (*SI Appendix*, Fig. S4). We found that the statistics derived from the 63 pine ILV networks were an outlier with respect to ILV metrics (e.g., average number of ILVs/networks, SD of number of ILVs/network), and within two SD of the mean (i.e., ~95% of the values) of the corresponding distributions with respect to budding sites metrics (*SI Appendix*, Fig. S4), indicating that the parameters used in such simulations cannot recapitulate the ILV networks seen in our tomograms.

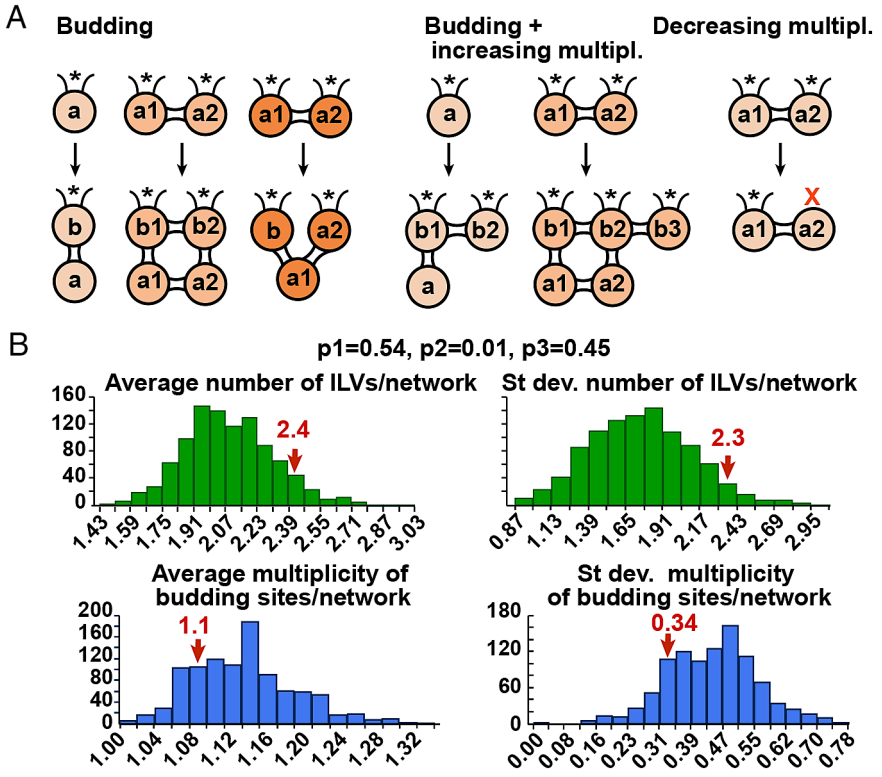

Fig. 4. Simulation of ILV network formation. (*A*) Diagrams depicting the three possible actions allowed to occur in the simulation. Asterisks indicate bridges still connected to the limiting membrane (budding site) and the letter and number inside each ILV reflects the order in which they were generated. (*B*) Distribution of the 1,000 repeats of 63 simulations each using the parameters p1 = 0.54, p2 = 0.01, p3 = 0.45. The red arrows indicate the values corresponding to the statistical analysis performed on the 63 ILV networks from the pine MVEs.

By performing further rounds of parameter sweeps and optimization (with 63 simulations per parameter set) for s1 to s3 as well as local search around p1 = 0.55, p2 = 0.1, and p3 = 0.35, we identified the parameter values s1 = 0.85, s2 = 0.05, and s3 = 0.1 as the best fit: In 10 out of 10 repeats, the null hypothesis was not rejected (Dataset S3), and p1 = 0.54, p2 = 0.01, p3 = 0.45 as a competitive parameter set ($P = 0.92$; $T^2 = 0.164$). With these optimized values for s1 to s3 and p1 to p3, we ran again 1,000 sets of 63 simulations each (Dataset S4). This time, the 63 pine ILV networks statistics fell within one SD of the mean of the distributions with respect to budding site metrics (average multiplicity of budding sites/network and corresponding SD) (Fig. 4*B*) and within two SD of the mean of the distributions with respect to the ILV metrics (average number of ILVs/network and corresponding SD) (Fig. 4*B*). While this is not a perfect fit, our model with these optimized parameters is much closer to resembling the ILV networks found in the pine MVE tomograms.

Taken together, the simulations suggest that in order to generate the ILV networks observed in pine MVEs, the limiting membrane favored continuous budding from the same site with a probability of ~54%. The probability of adding extra buds to form multiple budding sites was low (~1%), whereas existing ILV buds separated from the limiting membrane (elimination of bud and decrease in multiplicity) with ~45% probability.

Although we did not perform similar simulations for MVEs of all plant species, our parameter sweeps showed that slight changes in p1, p2, and p3 and s1, s2, and s3 can drastically affect the topology of the resulting ILV networks. Thus, it is reasonable to postulate that, compared to pine MVEs, relatively small increases in p2 and concomitant decreases in p3 at the limiting membrane resulted in the much larger proportion of multiple budding sites and more complex networks seen in flowering plants such as *Nymphaea* and *Arabidopsis*.

Diversification of ESCRT-III Subunits in Plants. Our simulation of membrane deformation during ILV formation indicates that changes in the properties of ESCRT-III filaments, such as filament curvature and increased membrane adhesion energy, could lead to the formation of concatenated networks and multiple budding sites. To explore the variation of ESCRT-III proteins among the organisms included in our tomographic analysis of MVEs, we collected amino acid sequences from all seven ESCRT-III subunits involved in endosomal budding. As there is no genome sequence information for any *Pteris* species, we searched for ESCRT-III-like proteins in another sequenced species of the same Pteridaceae family, *Ceratopteris richardii* (37). Although the genome of several species of *Pinus* has been sequenced, including the gigantic 25.4-Gb genome of *Pinus tabuliformis* (Chinese pine) (38), most remain poorly annotated, and we were unable to identify clear homologs of ESCRT-III subunits. Therefore, we queried the genome of *Cryptomeria japonica* within conifers to identify ESCRT-III components. In addition, we added *Oryza sativa* (rice) and *Medicago truncatula* as two flowering plant species with well-curated genomes. We performed BLAST searches using protein sequences of seven ESCRT-III subunits from budding yeast to *Arabidopsis* (*SI Appendix*, Fig. S5 and Table S3).

Although it is not possible to reliably infer physical properties of the ESCRT-III filaments based on the type and number of ESCRT-III isoforms in each species, our analysis showed some informative trends. As noticed previously, there is a general tendency for expansion of ESCRT-III subunits within plants (39), which could have led to isoforms with divergent properties. As plant lineages have undergone multiple events of duplication (40–42), it is not entirely surprising to find in plants multimember families of proteins that are represented by single members in animals and yeast. However, the different number of genes for each ESCRT-III subunit suggests that they may be under different types of selection. For example, whereas subunits like VPS20, VPS24, and VPS60 are represented by only 1 or 2 isoforms in all taxa under analysis, the IST1 subunit seems to have undergone multiple and drastic expansion events in green organisms. Whereas it is encoded by a single gene in humans and budding yeast (18, 43), *Chara* has five ISTL1-like proteins, *Ceratopteris* has 19 ISTL proteins, and *Arabidopsis*, 12 (ISTL1-12) (26).

As a way to validate that the formation of multiple budding sites in plants depends on the composition and remodeling of the ESCRT-III filaments, we analyzed MVE structural data of mutants lacking ESCRT-III subunits (CHMP1A and B, ISTL1) (8, 26) and/or LIP5 needed for SKD1-LIP5-mediated remodeling of ESCRT-III assemblies (26), in root or tapetal cells. In all cases, the mutants were able to generate budding sites and ILVs (Fig. 5*A*) but compared to wild type MVEs, the *chmp1, lip5, istl1 lip5* (both root and tapetum) mutant MVEs showed a striking reduction in multiplicity, with the *istl1 lip5* mutant root MVEs showing exclusively single budding sites (Fig. 5 *A*–*E*). Consistently, the *Arabidopsis* mutant MVEs also showed reduced number of bridges/ILV and overall ILV concatenation (Fig. 5 *B*, *D*, and *E*), similar to MVEs of early divergent land plants (Figs. 1*E* and 2*E*). This is consistent with the hypothesis that multiple budding sites in flowering plants require ESCRT-III assemblies of a specific composition and dynamics.

Discussion

We have shown that whereas ILV concatenation occurs in low frequency in nonplant organisms, not only is it widespread in plants, but has become increasingly prominent during the evolution of plant lineages. In addition, whereas early divergent plants almost exclusively form ILVs through single budding sites (with the exception of *Anthoceros*), multiple budding sites and complex ILV networks are predominant in late divergent groups, such as flowering plants. The biological consequences of these changes are unclear. One could speculate that both ILV concatenation and multiple budding enable more efficient internalization of cargo-loaded limiting membrane domains because a) vesiculation keeps progressing without halting for completion of membrane fission and b) multiple buds are internalized simultaneously. In addition, since membranous bridges internally coated with ESCRT proteins have been postulated to be effective barriers to the diffusion of cargo proteins (29), it is possible that both concatenation and multiple budding leading to more interconnecting ILV membranous bridges are also important for cargo retention.

Regardless of whether plant ILVs derive from multiple or single budding sites, their concatenation means that budding occurs persistently from the same domain at the limiting membrane, leading to interconnected ILVs. In fact, some of the linear ILV chains seen in species with predominant single budding sites suggest that the same site keeps on budding up to seven or eight times (*SI Appendix*, Figs. S1 and S3). ILV budding from distinct domains of the MVE surface has not only been observed in plants but also in animal cells (12). How exactly ESCRT-enriched domains are corralled and confined to a specific area of the MVE surface is currently unknown. In *Drosophila* endosomes, ESCRTs, cholesterol, and clathrin are important for the partition of the membrane receptor Notch into defined limiting membrane domains (44). In mammalian cells undergoing active EGFR internalization (45), ESCRT complexes associate with endosomes in transient waves that result in the formation of a single ILV (46).

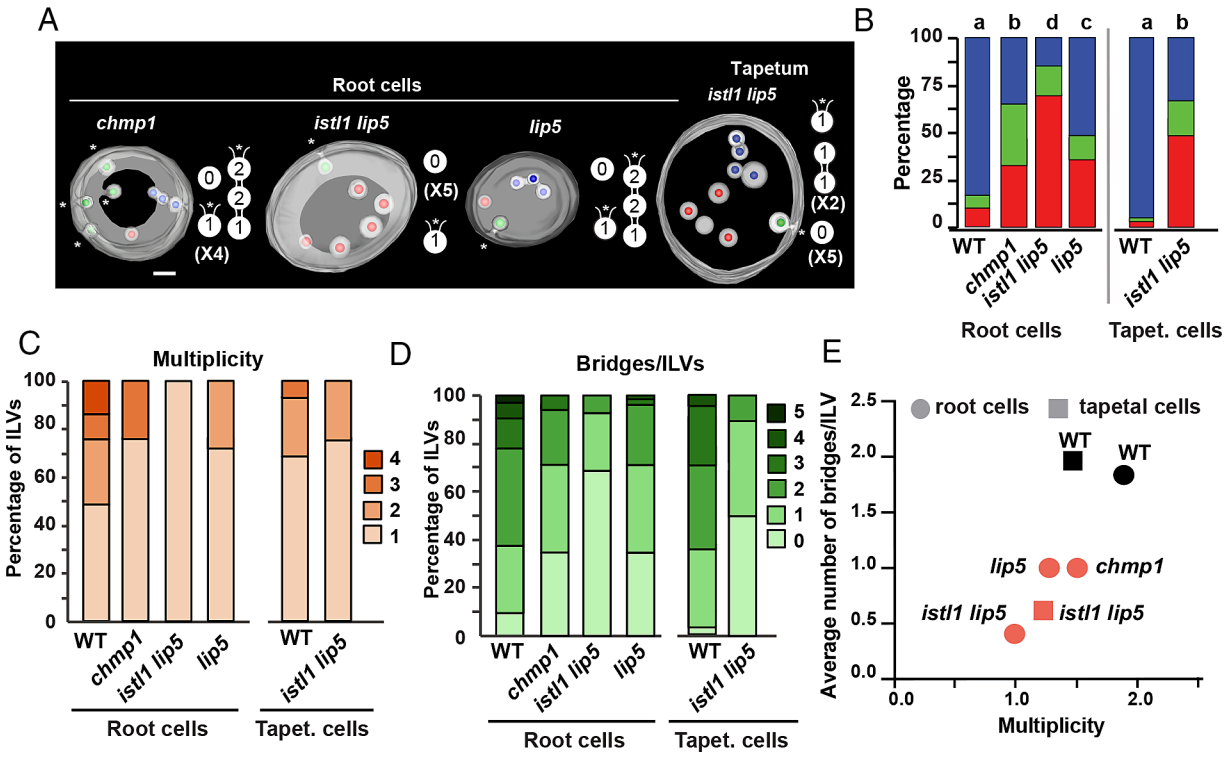

Fig. 5. Representative examples of MVEs of *Arabidopsis* mutants lacking ESCRT components. (*A*) Tomographic reconstruction of mutant MVEs and 2D ILV topologies. Asterisks indicate bridges still connected to the limiting membrane (budding site) and the number inside each ILV reflects the number of membranous bridges connected to it. Parentheticals indicate the number of times a given topology was found in the reconstructed MVE. (*B*) Percentage of concatenated, free, and single ILV buds across mutant MVEs. Different letters on graphs indicate significant difference ($P < 0.05$) calculated by a chi-squared test. (*C*) Percentage of budding sites with 1 to 4 interconnected ILV buds in wild type (WT) and mutant MVEs. (*D*) Percentage of ILVs associated with 0 to 5 membranous bridges. (*E*) Graph depicting the average number of bridges per ILV against the average number of ILVs in budding sites (multiplicity) in WT and mutant MVEs. (Scale bars, 50 mm).

However, successive rounds of ILVs' formation seem to concentrate in the same domain of the endosomal membrane (46), arguing for a delimitation of the ESCRT-mediated membrane budding activity. It is possible that both cargo and endosomal lipids promote the formation of fairly stable and large ESCRT-III-enriched domains on the endosomal membrane, promoting processive formation of concatenated ILVs.

Predominant ILV concatenation and multiple budding seem to be unique features of plant MVEs. Our simulations of MVE membranes and ESCRT-III filaments (Fig. 3) highlight the complexity of the required remodeling of ESCRT filaments and membrane shapes. Given enough cargo and ESCRT filaments on a domain of the limiting membrane, concatenation of a linear ILV chain from a single site can occur with three changes in the ESCRT filament properties (for example the formation of a linear chain, Fig. 3*C*, stage g). For a double budding site to form, though, the limiting membrane needs to be ruptured into a pore and the ESCRT filament properties (membrane adhesion energy, curvature, tilt) need to change at least six times (Fig. 3*C*, stages l and m). Using a complementary continuum model, our results suggest that membrane pore formation in double budding sites, as observed in the simulations, is plausible assuming typical membrane and ESCRT-III filament properties (Fig. 3*E*) and requires ESCRT-III filaments that strongly adhere to the membrane. Although we cannot assert that the formation of ILV networks in vivo require these minimal changes in the filament properties as seen in our simulations, it is clear that the formation of multiple budding sites requires more changes of the filament properties compared to all other topologies, in particular linear ILV chains. Therefore, our simulation predicts that linear chains and single buds should form more frequently than multiple budding sites in vivo, which is true in all plant species we have studied. In fact, we only detected multiple budding sites in the tomograms of MVEs from seed plants and hornworts. Moreover, our simulations predict that the filaments mediating the formation of multiple budding sites should be more dynamic and able to exhibit larger variations in their properties than those mediating the formation of single buds (*SI Appendix*, Table S2). It is tempting to speculate that this can be explained, at least in part, by the fact that there are many more ESCRT-III subunit isoforms in plants than in fungi and animals (*SI Appendix*, Fig. S5). Thus, it is reasonable to hypothesize that the diversification of ESCRT-III subunits in plants could have led to different MVE morphologies and membrane budding patterns.

Our computational simulations predict lower probabilities of increased multiplicity as budding sites become more complex. Thus, the probability of transitioning from a double into a triple budding site is lower than transitioning from a triple into a double budding site. This suggests that the higher the multiplicity, the lower the stability of the budding site. This is consistent with the predominance of single budding sites and linear chains in plant MVEs. However, our simulations also predict that small changes in the endosomal membrane patterns can drastically change the topology of networks, suggesting that relatively small variations in the ESCRT remodeling activity on the limiting membrane could explain the large variation of networks seen in plant species (*SI Appendix*, Fig. S1).

In general, ESCRT-III filament properties, such as curvature and membrane binding ability, depend on the subunit composition of the filament (23). Importantly, ESCRT-III filaments can undergo dynamic turnover driven by Vps4/SKD1 which can lead to a changing filament subunit composition. Hence, ESCRT-III filament properties can vary between species and over time depending on the exact subunit composition of the filament. In particular,

the changes in the property of ESCRT-III filaments that accompany membrane constriction and ILV budding in yeast depend on the progressive exchange of ESCRT-III subunits mediated by Vps4. Thus, the flat spirals generated by Snf7 polymerization (20) undergo a change in their tilt angle by the incorporation of Vps2, Vps24, and Did2, whereas the highly constricted spiral filaments are enriched in Did2/CHMP1 and Ist1 (23). The unique predicted behavior of ESCRT-III filaments during multiple budding of ILVs in plants could be explained by changes in Vps4/SKD1 activity and ESCRT-III subunit exchange rates and/or divergent property of ESCRT-III subunits, especially those expected to act in late steps of filament constriction, such as CHMP1 and IST1. Whereas the two CHMP1 proteins encoded by the *Arabidopsis* genome seem to have conserved functions with other eukaryotes (8), the biological implications of the large diversification of IST1-like proteins in *Arabidopsis* (26) and other plant species (*SI Appendix*, Fig. S5) are unclear. More research on plant ESCRT-III proteins and their filament dynamics will be needed to understand the molecular basis of multiple budding and ILV concatenation.

Materials and Methods

Sample Preparation for Transmission Electron Microscopy. Roots and other samples were high-pressure frozen in a Leica ICE using 0.1 M sucrose as cryoprotectant (47). Frozen samples were then freeze-substituted in 2% O_sO_4 in acetone at −80 °C overnight followed by gradual warm-up to room temperature. Samples were infiltrated in Eponate resin and polymerized at 60 °C degrees for 24 h. Semithick sections of 300 nm were mounted in carbon-coated slot grids, stained with 2% uranyl acetate and Reynold's lead citrate (2.6% lead nitrate and 3.5% sodium citrate, pH 12.0). Sections were then incubated in drops containing 10 nm gold fiducials to assist with the tomographic reconstruction. Images were collected in a Thermo Fisher Talos F200C G2 microscope operating at 200 kV, between 60° and −60° angles, at 1° angle intervals about two orthogonal axes using SerialEM (48). Images were collected using a Ceta 16 M 200 kV camera at a pixel size of 0.529 nm. Tomograms were calculated using the simultaneous iterative reconstruction technique (49), and the two single-axis tomograms were merged as previously described (50). Tomograms were displayed and analyzed with 3Dmod, the graphic component of the Image Modeler (IMOD) software package (51). The thinning factor for each tomogram was calculated and corrected for in the models. Measurements of MVE and ILV diameters as well as other morphometric analyses were done using IMOD.

Statistical Analyses. Data were visualized using GraphPad Prism 9 and Excel. The numbers of ILVs and MVEs contained in tomograms and considered for analysis were as follows: 112 ILVs from 3 MVEs in *S. cerevisiae*; 147 ILVs in 3 MVEs of *C. brownii;* 134 ILVs from 6 MVEs *in M. polymorpha*; 95 ILVs from 3 MVEs in *Anthoceros* sp.; 47 ILVs from 3 MVEs in *S. kraussiana; 64* ILVs in 3 MVEs from *P. cretica;* 505 ILVs from 10 MVEs in *P. resinosa;* 209 ILVs from 8 MVEs in *A. trichocarpa;* 251 ILVs from 5 MVEs in *A. thaliana* wild type roots; 183 ILVs in 5 MVEs in *A. thaliana* wild type tapetum; 13 ILVs from 4 MVEs of *istl1 lip5* mutant roots; 55 ILVs from 14 MVEs of *istl1 lip5* mutant tapetum; 34 ILVs from 8 MVEs in *chmp1* mutant roots; 64 ILVs from 12 MVEs in *lip5* mutant roots. To determine whether the mean number of bridges per vesicle was significantly different between species, the number of bridges of each vesicle in all MVEs collected were manually counted and added to a list for each species. These data were entered into *RStudio* where we ran the statistical tests. While this was discrete data (each number being a whole integer between 0 and 6), there was a large enough sample size that we were able to run ANOVA with post hoc Tukey tests to determine overall rejection of the null hypothesis as well as pairwise significance, using a P-value < 0.05 to indicate significance. We were also able to assume equal variance due to their only being a twofold difference in the variance extremes (*Chara* and *Nymphaea*).

To determine whether the proportions of vesicles that were concatenated, single buds, or free were significantly different between species and mutants, we categorized each individual vesicle in all MVEs collected as either "concatenated," "single," or "free" and added them to a tally for each species and mutant. We then ran pairwise chi-squared tests between each species/genotype on an online chi-squared test calculator (https://www.socscistatistics.com/tests/chisquare2/default2.aspx) to determine the P-value corresponding to the null hypothesis that the proportions were the same. We decided to reject the null hypothesis when the P-value was less than 0.05. Due to the high number of pairwise tests, we were concerned that some of the significance that we saw was due to random chance. Therefore, we corrected for this using false discovery rate analysis with q = 0.05, which did not detect any false positives in our results.

Molecular Dynamics Simulations. To simulate the endosomal membrane we used a previously developed coarse-grained model (32) in which a membrane bead represented a flat membrane patch. In our implementation of the model, the membrane consisted of $N_m = 16{,}560$ membrane beads. In the initial state, the membrane beads were distributed on a flat hexagonal lattice with the dimensions of 120 × 69 beads. Interactions between membrane beads were mediated by an anisotropic pair potential; we used the same parameterization as in the original publication, $r_{min} = 1.12\ \sigma$, $r_c = 2.6\ \sigma$, $\varepsilon = 4.34\ k_BT$, $\zeta = 4$, $\mu = 3$, and $\theta_0 = 0$, where σ was the length scale of the simulation and the diameter of a membrane bead (32). In our simulation, we assumed $\sigma \sim 2.3$ nm (33).

To simulate ESCRT filaments we used our previously devolved model (33). In the model, an ESCRT filament consisted of 69 subunits, each subunit formed from 3 ESCRT beads which were distributed along the shape of an equilateral triangle; thus, the filament consisted of $N_e = 207$ ESCRT beads in total. Each ESCRT bead had a bead diameter of $\sigma_{escrt} = \sigma$ so that the thickness of the ESCRT filament was ∼ 4.1 nm and the whole filament had a length of ∼159 nm. The beads of a subunit were bonded to the beads of a neighboring subunit via harmonic potentials, controlled by the bond strength $K_{bond} = 500\ k_BT$ and the rest length r_0. In the simulation, r_0 was related to the geometry of the ESCRT filament by the angle α between subunits and the tilt angle τ between the filament and the membrane (Fig. 3*A*). In the simulation, ESCRT beads exhibited volume exclusion, mediated by a cut and shifted 12-6 Lennard-Jones (LJ) potential, with the prefactor $\varepsilon_{ee} = 2\ k_BT$, the zero-crossing distance of the potential at $\sigma_{ee} = \sigma$ and the potential cutoff $r_{c\_ee} = 1.12\sigma$. ESCRT beads at the base of a subunit triangle were attracted to membrane beads, mediated by a 12-6 LJ potential with prefactor $\varepsilon_{ema} = 1.5 - 8\ k_BT$, zero-crossing distance $\sigma_{em} = (\sigma_{escrt} + \sigma)/2$ and cutoff $r_{c\_ema} = 1.12 \times 1.3\ \sigma_{em}$. ESCRT beads at the top of a subunit triangle exhibited volume exclusion, mediated by a 12-6 LJ potential with prefactor $\varepsilon_{emr} = 2\ k_BT$, zero-crossing distance σ_{em} and cutoff $r_{cemr} = 1.12\ \sigma_{em}$.

To model ILVs, we introduced $N_c = 2$ cargo beads with diameter $\sigma_{cargo} = 8\ \sigma$ which adhered to membrane beads, mediated by a 12-6 LJ potential with prefactor $\varepsilon_{cm} = 1.5\ k_BT$, zero-crossing distance $\sigma_{cm} = (\sigma_{cargo} + \sigma)/2$ and cutoff $r_{ccm} = 1.12 \times 1.5\ \sigma_{cm}$. Cargo beads interacted with each other through volume exclusion, mediated by a 12-6 LJ potential with energy $\varepsilon_{cc} = 3\ k_BT$, zero-crossing distance $\sigma_{cc} = \sigma_{cargo}$ and cutoff $r_{ccc} = 1.12\ \sigma_{cc}$. Cargo beads interacted with ESCRT beads through volume exclusion, mediated by a 12-6 LJ potential with prefactor $\varepsilon_{ce} = 3\ k_BT$, zero-crossing distance $\sigma_{ce} = (\sigma_{cargo} + \sigma_{escrt})/2$ and cutoff $r_{cce} = 1.12\ \sigma_{ce}$.

We effectively integrated the equations of motion in the *NpT* ensemble. By forcing $P = 0$, we mimicked vanishing membrane tension. All beads carried the same mass of $m = 1\ k_BT\ t_0^2/\sigma^2$, where t_0 is the simulation unit of time. We set the damping coefficient of the coupled Langevin thermostat to $\gamma = 1\ t_0$ and used a time step of $dt = 0.01\ t_0$. We used a simulation box with periodic boundary and dimensions $L_x = 120\ \sigma$, $L_y = 120\ \sigma$ and $L_z = 200\ \sigma$. To simulate and visualize the system, we use the Large-scale Atomic/Molecular Massively Parallel Simulator Molecular Dynamics (LAMMPS MD) simulation package (52) and Open Visualization Tool (OVITO) (53). The model parameters are summarized in *SI Appendix*, Table S1.

The parameters that define the membrane and cargo properties are held constant during the whole simulation. ESCRT filament parameters could change during the runtime. Changes in α occurred over a relatively long-time interval, because we expect that many subunits are involved. Changes in ε_{ema} and τ can occur over short time intervals, because we assumed that these changes could be driven by few subunits. We also assumed that the ESCRT filament can be cut into three parts during the simulation. The two necessary cuts of the filament are assumed to occur at the same time and distance, so that the resulting three filaments all have the same length (Fig. 3*B*). During this step, all filament properties are assumed to change instantaneously. All parameter values required to generate the seven final configurations and their intermediates displayed in Fig. 3*C* are included in *SI Appendix*, Table S2. Further details on the computational model can be found in *SI Appendix, Supplemental Methods*.

Simulation of ILV Network Formation. We used Matlab R2020a to run our simulations of ILV growth. Data were analyzed in Matlab and Microsoft Excel. All T^2-Hotelling tests were performed in Matlab using the *T2Hot2ihe* function. We use squared (0,1)-matrices of size n x n to represent the connectivity among the (n – 1) vesicles and between the vesicles and the limiting membrane. The simulation itself is discrete, i.e., starting from an initial ILV, the ILV grows step by step choosing one of three different events. At initialization, a simulated ILV has either one, two, or three budding sites, with probabilities s1, s2, and s3. Each simulation step, one of three events, namely i) budding, ii) adding a budding site, or iii) removing a budding site, is drawn randomly with probability p1, p2, and p3, respectively. If a budding event is drawn, the simulation does the following: In the presence of only one budding site, the budding happens at this site. In case the ILV has two budding sites, budding happens at one of the two (picked randomly) with probability s1/(s1 + s2) and otherwise at both budding sites. If the ILV has three or more budding sites, the probability for one, two, and three parallel budding events is s1, s2, and s3, respectively. Novel budding sites are always added with one or two parallel budding events (if it was not accompanied with a budding event, the new budding site would start a novel ILV, which is not allowed in our model): If the ILV has only one budding site, the simulation will add either one or two new budding sites plus one budding event at the existing budding site. The probability for the former is s2/(s2 + s3), while the probability of the latter is s3/(s2 + s3). If the ILV has more than one budding site, the simulation will add i) one new budding site plus one budding event with probability s2/(s2 + s3), or ii) one new budding site plus two budding events with probability s3/(2*(s2 + s3)), or iii) two new budding sites plus one budding event with equal probability s3/(2*(s2 + s3)). New budding sites are always connected to the buds that grew in parallel. The budding event sites are randomly chosen. A budding site is removed by randomly choosing and removing a connection between vesicles and the limiting membrane through corresponding changes in the matrix representation.

Each step, the resulting ILV is recorded, creating a history of the developing ILV network. The simulation stops either when the ILV is no longer connected to the limiting membrane (i.e., there is no active budding site) or when a maximum number of vesicles/buds has been reached. From the discrete set of ILV networks that were created during such a simulation, we randomly picked one as a "snapshot" and its properties (number of budding sites and number of vesicles), were captured for statistical analyses.

Data, Materials, and Software Availability. Electron tomogram files are deposited in EMPIAR under EMPIAR-12299 (54). All other data are included in the manuscript and/or supporting information.

ACKNOWLEDGMENTS. We would like to thank Janice Pennington for her support with electron tomography data collection, Dr. Ingrid Jordon-Thaden, director of the Botany Garden and Greenhouse of University of Wisconsin Madison, for her invaluable assistance collecting plant materials, Dr. Marie Trest for providing *Chara* specimens, and Dr. Nicholas Keuler for his advice on statistical analyses. We thank Charlie Hamilton for exploring the initial computational model. This work was supported by grant NSF MCB 2114603 and NIH 1S10OD026769-01 to M.S.O. F.F acknowledges support as a NOMIS Fellow from the NOMIS Foundation. A.Š. acknowledges ERC Starting Grant "NEPA" 802960.

Author affiliations: [a]Center for Quantitative Cell Imaging and Department of Botany, University of Wisconsin-Madison, Madison, WI 53706; [b]Institute of Science and Technology Austria, Klosterneuburg 3400, Austria; and [c]Department of Genetics, School of Medicine, University of Alabama-Birmingham, Birmingham, AL 35294-0024

1. J. Dettmer, A. Hong-Hermesdorf, Y. D. Stierhof, K. Schumacher, Vacuolar H+-ATPase activity is required for endocytic and secretory trafficking in *Arabidopsis*. *Plant Cell* **18**, 715–730 (2006).
2. J. Schöneberg, I. H. Lee, J. H. Iwasa, J. H. Hurley, Reverse-topology membrane scission by the ESCRT proteins. *Nat. Rev. Mol. Cell Biol.* **18**, 5–17 (2017).
3. D. J. Katzmann, M. Babst, S. D. Emr, Ubiquitin-dependent sorting into the multivesicular body pathway requires the function of a conserved endosomal protein sorting complex. *ESCRT-I.* **106**, 145–155 (2001).
4. M. Babst, D. J. Katzmann, E. J. Estepa-Sabal, T. Meerloo, S. D. Emr, ESCRT-III: An endosome-associated heterooligomeric protein complex required for MVB sorting. *Dev. Cell* **3**, 271–282 (2002).
5. M. Babst, D. J. Katzmann, W. B. Snyder, B. Wendland, S. D. Emr, Endosome-associated complex, ESCRT-II, recruits transport machinery for protein sorting at the multivesicular body. *Dev. Cell* **3**, 283–289 (2002).
6. L. Schlösser, C. Sachse, H. H. Low, D. Schneider, Conserved structures of ESCRT-III superfamily members across domains of life. *Trends Biochem. Sci.* **48**, 993–1004 (2023).
7. L. Christ, C. Raiborg, E. M. Wenzel, C. Campsteijn, H. Stenmark, Cellular functions and molecular mechanisms of the ESCRT membrane-scission machinery. *Trends Biochem. Sci.* **42**, 42–56 (2017).
8. C. Spitzer *et al.*, The ESCRT-related CHMP1A and B proteins mediate multivesicular body sorting of auxin carriers in *Arabidopsis*. and are required for plant development. *Plant Cell* **21**, 749–766 (2009).
9. C. Spitzer *et al.*, The endosomal protein CHARGED MULTIVESICULAR BODY PROTEIN1 regulates the autophagic turnover of plastids in *Arabidopsis*. *Plant Cell* **27**, 391–402 (2015).
10. T. J. Haas *et al.*, The Arabidopsis. AAA ATPase SKD1 is involved in multivesicular endosome function and interacts with its positive regulator LYST-INTERACTING PROTEIN5. *Plant Cell* **19**, 1295–1312 (2007).
11. A. Katsiarimpa *et al.*, The deubiquitinating enzyme AMSH1 and the ESCRT-III subunit VPS2.1 are required for autophagic degradation in *Arabidopsis*. *Plant Cell* **25**, 2236–2252 (2013).
12. E. B. Frankel *et al.*, Ist1 regulates ESCRT-III assembly and function during multivesicular endosome biogenesis in Caenorhabditis elegans embryos. *Nat. Commun.* **8**, 1439 (2017).
13. C. Gao *et al.*, A unique plant ESCRT component, FREE1, regulates multivesicular body protein sorting and plant growth. *Curr. Biol.* **24**, 2556–2563 (2014).
14. A. Katsiarimpa *et al.*, The Arabidopsis. deubiquitinating enzyme AMSH3 interacts with ESCRT-III subunits and regulates their localization. *Plant Cell* **23**, 3026–3040 (2011).
15. H. Wang *et al.*, Rapid depletion of ESCRT protein Vps4 underlies injury-induced autophagic impediment and Wallerian degeneration. *Sci. Adv.* **5**, eaav4971 (2019).
16. Y. Olmos, The ESCRT machinery: Remodeling, repairing, and sealing membranes. *Membranes* **12**, 633 (2022).
17. S. M. Rue, S. Mattei, S. Saksena, S. D. Emr, Novel ist1-did2 complex functions at a late step in multivesicular body sorting. *Mol. Biol. Cell* **19**, 475–484 (2008).
18. C. Dimaano, C. B. Jones, A. Hanono, M. Curtiss, M. Babst, Ist1 regulates Vps4 localization and assembly. *Mol. Biol. Cell* **19**, 465–474 (2008).
19. N. Chiaruttini *et al.*, Relaxation of loaded ESCRT-III spiral springs drives membrane deformation. *Cell* **163**, 866–879 (2015).
20. Q. T. Shen *et al.*, Structural analysis and modeling reveals new mechanisms governing ESCRT-III spiral filament assembly. *J. Cell Biol.* **206**, 763–777 (2014).
21. N. Jukic, A. P. Perrino, F. Humbert, A. Roux, S. Scheuring, Snf7 spirals sense and alter membrane curvature. *Nat. Commun.* **13**, 2174 (2022).
22. X. Jiang *et al.*, Modelling membrane reshaping by staged polymerization of ESCRT-III filaments. *PLoS Comput. Biol.* **18**, e1010586. (2022).
23. A. K. Pfitzner *et al.*, An ESCRT-III polymerization sequence drives membrane deformation and fission. *Cell* **182**, 1140–1155.e1118 (2020).
24. A. González Solís, E. Berryman, M. S. Otegui, Plant endosomes as protein sorting hubs. *FEBS Lett.* **596**, 2288–2304 (2022).
25. I. Azmi *et al.*, Recycling of ESCRTs by the AAA-ATPase Vps4 is regulated by a conserved VSL region in Vta1. *J. Cell Biol.* **172**, 705–717 (2006).
26. R. Buono *et al.*, Role of SKD1 regulators LIP5 and IST1-LIKE 1 in endosomal sorting and plant development. *Plant Physiol.* **171**, 251–264 (2016).
27. J. H. Leebens-Mack *et al.*, One thousand plant transcriptomes and the phylogenomics of green plants. *Nature* **574**, 679–685 (2019).
28. J. R. Edgar, E. R. Eden, C. E. Futter, Hrs- and CD63-dependent competing mechanisms make different sized endosomal intraluminal vesicles. *Traffic* **15**, 197–211 (2014).
29. R. A. Buono *et al.*, ESCRT-mediated vesicle concatenation in plant endosomes. *J. Cell Biol.* **216**, 2167–2177 (2017).
30. K. Goodman *et al.*, ESCRT components ISTL1 and LIP5 are required for tapetal function and pollen viability. *Plant Cell* **33**, 2850–2868 (2021).
31. C. Liu *et al.*, AP1/2β-mediated exocytosis of tapetum-specific transporters is required for pollen development in *Arabidopsis thaliana*. *Plant Cell* **34**, 3961–3982 (2022).
32. H. Yuan, C. Huang, J. Li, G. Lykotrafitis, S. Zhang, One-particle-thick, solvent-free, coarse-grained model for biological and biomimetic fluid membranes. *Phys. Rev. E* **82**, 011905. (2010).
33. L. Harker-Kirschneck, B. Baum, A. E. Šarić, Changes in ESCRT-III filament geometry drive membrane remodelling and fission in silico. *BMC Biol.* **17**, 82 (2019).
34. F. Frey, F. Ziebert, U. S. Schwarz, Stochastic dynamics of nanoparticle and virus uptake. *Phys. Rev. Lett.* **122**, 088102 (2019).
35. M. Deserno, Fluid lipid membranes: From differential geometry to curvature stresses. *Chem. Phys. Lipids* **185**, 11–45 (2015).
36. J. Moser von Filseck *et al.*, Anisotropic ESCRT-III architecture governs helical membrane tube formation. *Nat. Commun.* **11**, 1516 (2020).
37. D. B. Marchant *et al.*, Dynamic genome evolution in a model fern. *Nat. Plants* **8**, 1038–1051 (2022).
38. S. Niu *et al.*, The Chinese pine genome and methylome unveil key features of conifer evolution. *Cell* **185**, 204–217.e214 (2022).
39. V. Winter, M.-T. Hauser, Exploring the ESCRTing machinery in eukaryotes. *Trends Plant Sci.* **11**, 115–123 (2006).
40. N. Panchy, M. Lehti-Shiu, S. H. Shiu, Evolution of gene duplication in plants. *Plant Physiol.* **171**, 2294–2316 (2016).
41. J. W. Clark, Genome evolution in plants and the origins of innovation. *New Phytol.* **240**, 2204–2209 (2023).
42. K. Vanneste, G. Baele, S. Maere, Y. Van de Peer, Analysis of 41 plant genomes supports a wave of successful genome duplications in association with the Cretaceous-Paleogene boundary. *Genome Res.* **24**, 1334–1347 (2014).

43. M. Bajorek *et al.*, Biochemical analyses of human IST1 and its function in cytokinesis. *Mol. Biol. Cell* **20**, 1360–1373 (2009).
44. H. Shimizu, S. Hosseini-Alghaderi, S. A. Woodcock, M. Baron, Alternative mechanisms of Notch activation by partitioning into distinct endosomal domains. *J. Cell Biol.* **223**, e202211041 (2024).
45. K. B. Quinney *et al.*, Growth factor stimulation promotes multivesicular endosome biogenesis by prolonging recruitment of the late-acting ESCRT machinery. *Proc. Natl. Acad. Sci. U.S.A.* **116**, 6858–6867 (2019).
46. E. M. Wenzel *et al.*, Concerted ESCRT and clathrin recruitment waves define the timing and morphology of intraluminal vesicle formation. *Nat. Commun.* **9**, 2932 (2018).
47. J. Pennington, M. S. Otegui, Imaging the plant cytoskeleton by high-pressure freezing and electron tomography. *Methods Mol. Biol.* **2604**, 89–102 (2023).
48. D. N. Mastronarde, Automated electron microscope tomography using robust prediction of specimen movements. *J. Struct. Biol.* **152**, 36–51 (2005).
49. P. Gilbert, Iterative methods for the three-dimensional reconstruction of an object from projections. *J. Theor. Biol.* **36**, 105–117 (1972).
50. D. N. Mastronarde, Dual-axis tomography: An approach with alignment methods that preserve resolution. *J. Struct. Biol.* **120**, 343–352 (1997).
51. J. R. Kremer, D. N. Mastronarde, J. R. McIntosh, Computer visualization of three-dimensional image data using IMOD. *J. Struct. Biol.* **116**, 71–76 (1996).
52. A. P. Thompson *et al.*, LAMMPS - a flexible simulation tool for particle-based materials modeling at the atomic, meso, and continuum scales. *Comput. Phys. Commun.* **271**, 108171 (2022).
53. A. Stukowski, Visualization and analysis of atomistic simulation data with OVITO–the open visualization tool. *Modell. Simul. Mater. Sci. Eng.* **18**, 015012 (2010).
54. E. Weiner *et al.*, Electron tomograms of high-pressure frozen-freeze substituted multivesicular endosomes. EMPIAR. https://www.ebi.ac.uk/empiar/EMPIAR-12299/. Deposited 23 September 2024.